Advanced Composites and Hybrid Materials (2026) 9:278
https://doi.org/10.1007/s42114-026-01831-6

RESEARCH

3D-printed multiresonant sensor for ultra-low frequency vibration monitoring

J. Gómez-Hurtado[1,2] · D. Liguori[1,2] · I. Royo-Silvestre[1,2] · D. Gandía[1,2] · J. M. Algueta-Miguel[3,4] · J. Hernández-Saz[5] · C. Gómez-Polo[1,2] · E. Garaio[1,2] · A. López-Ortega[1,2] · J. J. Beato-López[1,2]

Received: 19 February 2026 / Revised: 2 April 2026 / Accepted: 24 April 2026
© The Author(s) 2026

Abstract

A proof-of-concept accelerometer for ultra-low and low-frequency vibration sensing is presented. The device integrates a high-sensitivity Giant Magnetoimpedance (GMI) sensor with a 3D-printed magnetized resonant structure, based on the low Young's modulus of polymers and the geometric versatility of additive manufacturing to explore its potential as an alternative sensing approach to conventional piezoelectric sensors in the low-frequency regime. The sensing architecture consists of a serpentine-like PLA resonator combined with a self-manufactured hard magnetic composite of cobalt-doped ferrite nanoparticles $Co_xFe_{3-x}O_4$ embedded in a polycaprolactone matrix. Finite Element Method (FEM) simulations were utilized to optimize the geometry, ensuring fundamental resonant modes within the targeted ultra-low-frequency range. Experimental results demonstrate a primary resonant response between 8 and 11 Hz, maintaining high detection reliability even at peak-to-peak acceleration levels as low as 0.05 g. Furthermore, the sensing performance is shown to be highly tunable by adjusting the magnetic nanoparticle loading or remanent magnetization, while the addition of proof masses allows for post-fabrication frequency shifting down to 4.3 Hz. This work demonstrates a low-cost, contactless, and reconfigurable platform for sensing ultra-low and low-frequency vibrations even at low acceleration levels.

Highlights

- A proof-of-concept device for ultra-low frequency vibration sensing is presented.
- The device combines additive manufacturing with Giant Magnetoimpedance (GMI) sensing for contactless detection.
- Tailored cobalt-doped ferrite nanoparticles enable tunable magnetic response and sensing performance.
- Reliable vibration detection was demonstrated down to 0.05 g in the 8–11 Hz range.
- Post-fabrication addition of proof masses allows the fundamental resonance to be shifted as low as 4.3 Hz.

Keywords Giant Magnetoimpedance (GMI) · 3D printing · Magnetic nanoparticles · Ultra-low frequency · Vibration sensors · Magnetic composite materials · Resonant structures.

1 Introduction

Three-dimensional (3D) printing is a manufacturing technique in which digital models are built and fabricated by automated equipment that deposits material layer by layer [1, 2], offering significant advantages over conventional methods, such as waste minimization and the efficient creation of complex structures [3, 4]. Particularly, Fused Deposition Modeling, FDM, enables the fabrication of smart materials by extruding heated thermoplastics through computer-controlled nozzles, allowing for precise spatial control over material composition [5, 6]. By strategically embedding functional fillers into polymeric matrices, FDM

✉ J. J. Beato-López
juanjesus.beato@unavarra.es

1 Department os Sciences, UPNA, Pamplona, Navarra, Spain

2 Institute for Advanced Materials and Mathematics, UPNA, INAMAT 2, Pamplona, Navarra, Spain

3 Department of Electrical and Electronic Engineering and Communications (IEEC), UPNA, Pamplona, Navarra, Spain

4 Institute of Smart Cities, ISC, UPNA, Pamplona, Spain

5 Department of Engineering and Materials Science and Transportation, University of Seville, Seville, Spain

Published online: 29 April 2026

facilitates the fabrication of complex architectures with programmable gradients for sensing, remote actuation, and controlled release [7–9] among other responses. An example is the design of smart magnetic 3D-printed composites obtained by embedding magnetic nanoparticles (MNPs) into polymer matrices [10, 11], leading to tailored multifunctional behavior that can be programmed within a single printed part [12–14].

Within this framework, hard MNPs, i.e., those with remanent magnetization, enable the development of 3D-printed magnetized composites that sustain their magnetization in the absence of an external field. This feature opens the way for multipurpose applications, among them, vibration characterization in the low ($\leq$ 100 Hz) [15, 16] and ultra-low ($\leq$ 10 Hz) frequency range [15, 17] through their strategic integration in polymeric resonant structures. This capability represents a technologically relevant application, since ultra-low and low-frequency vibrations are ubiquitous and originate from multiple sources, including civil infrastructures, industrial machinery, and human motion [15, 18, 19]. Such characterization is particularly relevant for applications like Structural Health Monitoring (SHM) [20], where these vibrations are commonly accompanied by low acceleration levels [21, 22].

Characterization of mechanical vibrations mainly consists of the determination of oscillation motion amplitude (acceleration) and frequency [23, 24]. This task is fundamentally performed by fiber optic sensors and accelerometers [19, 25–28]. While, fiber optic sensors enable continuous, high-resolution monitoring and offer advantages such as high sensitivity, reliability, stability, compact size, and immunity to electromagnetic interference [29, 30], their widespread adoption remains limited due to factors such as high cost, mechanical fragility, installation complexity, and operational challenges for end users [29, 30]. On the other hand, piezoelectric accelerometers can be considered among the most common sensors in vibration characterization [31–33] since they provide compactness, a wide operational range and cost-efficiency [19, 28, 34]. However, their application, especially in the ultra-low frequency regime, is restricted by their limited response in this frequency range [32]. This performance decay arises from inherent properties of active piezoelectric materials, mainly, charge leakage [32, 35] and high noise rate [31, 36] (particularly in piezoelectric Microelectromechanical systems, MEMS), making these sensors unable to measure static or quasi-static vibrations [32]. Moreover, the high intrinsic resonance frequency of active materials complicates their matching to the natural frequencies of ultra-low and low-frequency vibration sources [18, 37–39]. Thus, the adaptation of piezoelectric technology to ultra-low-frequency sensing requires sophisticated material optimization and complex signal compensation [31, 32]. A great variety of lower detection thresholds can be found depending on the active material and associated electronics, for instance, in [40], a signal degradation has been reported starting at 5 Hz in a commercial sensor. Currently, Integrated Electronics Piezo-Electric (IEPE) and polymeric sensors (such as Polyvinylidene Fluoride, PVDF) represent the primary commercial and research standards in this regimen. IEPE sensors, while offering low-noise performance, rely on Lead Zirconate Titanate (PZT) with the presence of toxic lead (Pb) [41]. Additionally, these devices exhibit amplitude and phase deviations at low frequencies [42], which requires the implementation of demanding and specific signal conditioning and calibration procedures [31, 42] that hinder their practical use below 1 Hz [31, 42]. Despite this, IEPE devices reaching sub-Hertz limits (0.008–1 Hz) are available, displaying large proof masses (100–1000 g) and high costs, while more compact models (0.5–10 g) that approach 0.5–1 Hz still carry substantial associated costs. Alternatively, polymeric piezoelectrics, such as polyvinylidene fluoride (PVDF), have emerged as flexible, additive-manufacturing-compatible alternatives [43, 44]. Nevertheless, they require complex activation processes during or after fabrication/impression [45, 46] yielding a lower piezoelectric response and increased noise density than PZT-based devices [43]. These limitations reveal that accurate, low-frequency measurements remain technically and economically challenging [31, 36], stating the need for lighter, simpler, and cheaper choices [47] capable of operating in the 0.1–10 Hz range while maintaining a lightweight profile and a low-cost architecture.

In this scenario, magnetic-based sensing has attracted significant attention due to its capability to detect small displacements without requiring direct mechanical contact. Among magnetic phenomena, the Giant Magnetoimpedance (GMI) effect stands out due to its high sensitivity [48]. This effect involves significant changes in the high-frequency electrical impedance of a soft magnetic conductor upon exposure to an external magnetic field [48], such as those generated by embedded MNPs. Beyond its demonstrated capacity in the static contactless detection of MNPs [49–51] and development of bulk-magnet linear accelerometers [23], the GMI effect emerges as a promising principle for vibration monitoring through the dynamic detection of the MNPs' remanent magnetization during oscillatory motion. In addition to this, the development of appropriate resonant structures in the ultra-low and low-frequency range represents a significant design challenge, often requiring complex, time-consuming, and costly procedures [18, 37, 39]. To address this, our approach exploits the inherently low Young modulus [37] of polymers and the geometric versatility of additive manufacturing [52], enabling the efficient fabrication of resonant polymeric structures within

the targeted frequency range through a simple and low-cost process that simultaneously facilitates the localized integration of magnetized composites supporting magnetic-based vibration characterization.

Building on the above, a proof-of-concept accelerometer for ultra-low and low-frequency vibration sensing is presented. The system combines a GMI sensor with a 3D-printed magnetized resonant structure fabricated from two different materials: commercial polylactic acid (PLA) filament and a self-manufactured hard magnetic composite combining polycaprolactone (PCL) polymer embedded with cobalt-doped ferrite MNPs. The proposed device operates on a hybrid magneto-mechanical principle, where 3D-printed polymeric architectures serve as both a mechanical amplifier and a magnetic signal generator. In this configuration, the polymeric resonator is tailored to match target vibration frequencies, inducing a resonant mechanical response that amplifies the oscillation amplitude of the integrated magnetic composite. This displacement causes a periodic variation in the relative distance between the magnetized composite and the GMI sensor. Consequently, the dynamic displacement is transduced into a measurable electrical impedance modulation, enabling contactless vibration monitoring through the coupling of elastic deformation and magnetic field intensity variations. According to this, different sensor devices containing different MNP compositions and filling factors were fabricated and submitted to vibrational tests. The optimal system exhibited a resonant behavior in the range of 8–11 Hz, even at low peak-to-peak acceleration levels (0.05 g = 0.49 m/s^2). Furthermore, the addition of proof masses reduced the fundamental resonance to 4.3 Hz, enabling vibration characterization within the ultra-low-frequency range $\leq$ 10 Hz [16, 18]. The proposed approach demonstrates the feasibility of combining additive manufacturing with GMI sensing to develop low-cost, easy assembly and replacement and tunable sensor devices for ultra-low and low-frequency vibration characterization.

2 Materials and methods

2.1 Materials

Cobalt (II) chloride ($CoCl_2$, ≥ 99%), iron(III) acetylacetonate (Fe(acac)3, 99.99%), oleic acid (OA, 90%), oleylamine (ONH_2, 70%), benzyl ether (Bz_2O, 98%) and dichloromethane (DCM, 98%) were purchased from Merck KGaA (Sigma-Aldrich). Ethanol was obtained from Panreac S.A. The solvents were used as received without further purification. Polylactic acid (PLA, Mw, ≈ 20.000) and polycaprolactone (PCL, Mw, ≈ 50.000) polymers were purchased from RSpro and Polymorph, respectively.

2.2 Cobalt-doped ferrite MNPs synthesis and characterization

20 nm cuboctahedral cobalt-doped ferrite nanoparticles were synthesized through thermal decomposition of organometallic compounds in high-boiling solvent containing OA and ONH_2 as stabilizing surfactants [53]. In a typical synthesis, 12 mmol of metal precursors ($Fe(acac)_3$ and $CoCl_2$) were dissolved in a solution containing 1.8 mmol of OA, 2.4 mmol of ONH_2, and 20 mL of Bz_2O in a 100 mL three-neck round-bottomed flask. Initially, the mixture was degassed by bubbling N_2 at 100 °C for 20 min, and then it was heated up to the desired decomposition temperature (270 °C), setting heating rate (1 °C/min), nucleation step, and digestion time (15 min) to control the final particle size. During the heating and digestion processes, the mixture was exposed to an N_2 flow. Finally, the flask was removed from the heating mantle and allowed to cool under an inert atmosphere. All nanoparticles were washed by several cycles of coagulation with ethanol, centrifugation at 5000 rpm, disposal of supernatant solution, and redispersion in chloroform. Three different samples were synthesized by varying the Co/Fe precursor ratios to 0.4, 0.6, and 1.3, corresponding to the x = 0.32, 0.58, and 0.78 stoichiometries, respectively, where x refers to $Co_xFe_{3-x}O_4$.

2.3 Magnetic composite fabrication

The different self-manufactured magnetic composites were fabricated following a slightly modified solid casting process [11]. First, PCL was dissolved in 10 mL of DCM under mechanical stirring at room temperature. Once the polymer was fully dissolved and the resulting colorless solution became noticeably more viscous, the corresponding amount of MNPs (filling factors 5 and 20%wt) was incorporated. The mixture was continuously stirred until complete solvent evaporation was achieved.

2.4 Structural and morphological characterization of MNPs and magnetic composite

The structural characterization of the MNPs was performed by X-ray powder diffraction (XRD) using a Bruker D8 ADVANCE ECO diffractometer equipped with Cu Kα radiation, operating at 40 kV and 25 mA. Diffraction patterns were collected in a two-theta range from 20° to 70°, with a step size of 0.02° and scan speed of 0.2 s per step. The obtained patterns were analyzed by the Rietveld refinement using the MAUD program [54].

The relative concentrations of cobalt and iron were measured by inductively coupled plasma atomic emission spectroscopy (ICP) using an Agilent Vista-MPX instrument.

Approximately 1.5 mg of each MNPs sample was dissolved in 0.6 mL of freshly prepared *aqua regia* (1:3 nitric acid to hydrochloric acid ratio). The resulting solution was diluted to 25 mL with Milli-Q water and subsequently used for ICP analysis.

The morphologies of the MNPs and their distribution into the magnetic composite were investigated by scanning electron microscopy (SEM, Zeiss EVO), high-resolution SEM (HR-SEM, Zeiss CrossBeam 350), and energy dispersive X-ray spectroscopy (EDX).

Three-dimensional characterization was performed via FIB-SEM tomography using a Thermo Fisher Scientific Scios 2 DualBeam system, featuring an electron beam resolution of 1.4 nm at 1 keV and an accelerating voltage range of 200 V–30 kV. Signal detection was managed by a Trinity detector system, incorporating both segmented lower and upper in-lens detectors alongside in-column sensors. For material removal, the ion beam was operated at an accelerating voltage of 30 kV, utilizing a sequential milling process to remove layers. High-resolution SEM micrographs were acquired following each milling step to capture the newly exposed surfaces with optimized contrast. Alignment of the acquired image stack was performed in Avizo software via a sum of squared differences algorithm, excluding rotation correction.

The magnetic properties of the MNPs and magnetic composites were measured on tightly packed powder samples and 0.2 × 0.2 cm pieces of the composite using a lab-made vibrating sample magnetometer (VSM) [55] with a maximum applied field of 1.5 T.

2.5 Magnetized resonant structure 3D-printing

The complete magnetized resonant structures were fabricated by 3D printing using a BIO V1 bioprinter (REGEMAT 3D, Spain) equipped with interchangeable extrusion modules that allow the processing of both polymer filaments and composite materials. This configuration enabled the successive printing of the resonant structure and the magnetic composite within a single integrated manufacturing workflow. First, the resonant structure body was printed using commercial PLA filament. Subsequently, the magnetic component was printed directly onto the resonator using the previously prepared PCL-based magnetic composite. For this purpose, the composite was dried, cut into small granules (0.5–5 mm in diameter), and fed into the extrusion head in pellet form. Printing parameters were controlled through the REGEMAT3D Designer software, with a layer height of 0.25 mm, a nozzle temperature of 200 °C, and 20% infill density, ensuring adequate adhesion between layers and mechanical integrity of the printed parts.

2.6 FEM–based design of the resonant structure

Numerical simulations based on the Finite Element Method (FEM) [56] were carried out to define the geometry of a 3D-printed PLA polymeric resonator to operate within the ultra-low and low-frequency range. The resonant frequencies were estimated by solving the following linear elasticity partial differential equation (PDE):

$$C\prime_{i,j,k,l}\frac{\partial u_k}{\partial x_j \partial x_l} = -\rho\ \omega^2 u_i \qquad (i,j,k,l = x,y,z) \tag{1}$$

where u_k are the components of the displacement vector, $C\prime_{i,j,k,l}$ is the unsymmetrized stress tensor, ρ is the structure mass density and ω is the oscillation angular frequency of the vibration source. Here, the displacement vector u_k is assumed to be zero at the surfaces in contact with the vibration source (Dirichlet boundary condition).

To solve the above-stated equation, Eq. (1) was transformed to the following eigenvalue and eigenvector equation [57]:

$$K_{r,s}\mathrm{u}_s^m = \lambda^m M_{r,s}\,\mathrm{u}_s^m \tag{2}$$

where $K_{r,s}$ and $M_{r,s}$ are the stiffness and mass FEM matrices, u_s^m is the m-th eigenvector at s-th node and λ^m is the m-th eigenvalue. From the eigenvalues λ^m in Eq. (2), the resonant frequencies of the m-th vibration mode, f^m, were calculated as:

$$f^m = \frac{1}{2\pi}\sqrt{-\frac{\lambda^m}{\rho}} \tag{3}$$

From the u_s^m eigenvectors in Eq. 2, the displacements corresponding to the m-th vibration modes at the s-th node were obtained. The assembly of the mass and stiffness matrices [58], as well as the solution of the eigenvalue problem, were performed using an Octave-based script (https://octave.org/).

The geometry of the resonant structure was designed using FreeCAD (https://www.freecad.org/index.php). In order to generate the mesh required for the FEM analysis, the open-source software Gmsh (https://gmsh.info/) was used, loading the FreeCAD geometry as a STEP (Standard for the Exchange of Product model data) formatted file.

Regarding the resonator material properties, isotropic linear elasticity was considered. Then, the unsymmetrized stress tensor in Eq. (1) becomes:

$$C\prime_{i,j,k,l} = \frac{E}{2(1+\nu)}\delta_{\mathrm{i,j}}\delta_{\mathrm{k,l}} + \frac{E}{(1+\nu)(1-2\nu)}(\delta_{\mathrm{i,k}}\delta_{\mathrm{j,l}} + \delta_{\mathrm{i,l}}\delta_{\mathrm{j,k}}) \tag{4}$$

where E is the Young's modulus and ν is the Poisson's ratio of the resonant structure material. Concretely, the bulk material properties considered for PLA were: density of $\rho = 1200\, kg \cdot m^{-3}$, Young's modulus of E = 3 GPa and Poisson's ratio of ν = 0.38 [59].

2.7 GMI sensor characterization

The GMI position sensor core was an amorphous wire with nominal composition $(Co_{0.94}\, Fe_{0.06})_{72.5}Si_{12.5}B_{15}$ and a mean diameter of 140 μm obtained by the "in-rotating-water-quenching" technique [60]. To enhance its sensitivity to low magnetic fields, a 5 cm wire was submitted to a thermal-torsional treatment similar to that described in [50]. A 3 cm subsection of the treated wire was employed as the GMI sensing element of the vibration sensor. The operating conditions that maximize the GMI effect on the wire, namely the driving frequency, f_{GMI}, and peak-to-peak current, I_{pp}, were determined using a standard optimization procedure [50]. The resulting optimal parameters were f_{GMI} = 300 kHz and I_{pp} = 20 mA. These excitation conditions remained constant in all experiments. To optimize device response, the GMI wire longitudinal axis was aligned with that of the magnetic composite.

2.8 Ultra-low and low-frequency vibration tests

The performance of the printed accelerometers (magnetized resonant structure and GMI sensor) was evaluated by fixing them onto an electrodynamic shaker (LDS V201) driven by a low-frequency AC signal generated with a function generator (AFG 310, Sony Tektronix) and an AC linear power amplifier (LDS, LPA100 Brüel and Kjaer). Then, each accelerometer was subjected to sinusoidal ultra-low and low-frequency vibrations under both controlled excitation frequency, $f = \frac{\omega}{2\pi}$ (with ω as angular frequency) and peak-to-peak acceleration, a, adjusted by a commercial accelerometer (PCD, 352C33) with negligible mass loading effects (1 g = 9.8 m/s^2 corresponding to 100 mV peak-to-peak). Concretely, the excitation frequency was swept within the range of 4 to 35 Hz, while peak-to-peak acceleration was fixed at 0.05, 0.1, 0.2, and 0.3 g in each test. An initial relative distance, x_{res} = 5 mm, between the GMI and the magnetized resonant structure was selected. In parallel, the peak-to-peak voltage signals of both the commercial and 3D printed accelerometers, V_{out}, were simultaneously acquired with an oscilloscope (Picoscope 3403D), together with the vibration frequency of the magnetized composite. The accelerometers' related signals were acquired by means of a homemade analog electronic interface [23] based on a double passive envelope detector (positive and negative) followed by differential amplification. To examine the statistical robustness and reproducibility of the proposed devices, three identical magnetized resonant units (n = 3) were fabricated and characterized, enabling a comprehensive study of both frequency and voltage (sensitivity) variability in relevant resonant regions. Finally, preliminary 1-day continuous working tests (20% wt) were conducted at 9 Hz and 0.5 g (exceeding the standard experimental range) to assess the device's stability, where both frequency and voltage were monitored.

2.9 GMI sensor response characterization

To characterize the intrinsic voltage response of the GMI sensor to vibrations of the magnetic composite, a calibration procedure was carried out using magnetic composites with two different MNPs concentrations, 5 and 20 wt%. For this purpose, each magnetic composite was sequentially placed directly on the shaker platform, while the polymeric resonator was mechanically isolated and did not participate in the motion. The GMI sensor was positioned at a fixed distance x_{res} = 5 mm from the top part of the magnetic composite and remained fixed at rest out of the shaker platform (not submitted to vibration). The system was excited at a fixed frequency of 9 Hz, and the output voltage V_{out} of the GMI sensor was recorded while the applied peak-to-peak acceleration was varied between 0.05 and 3 g. Under these conditions, the magnetic composite element follows the imposed sinusoidal motion of the shaker, providing a direct evaluation of the GMI response to the oscillatory motion of the magnetic element, without the influence of mechanical resonance effects. Since both the excitation frequency ω and the acceleration amplitude, a, applied to the shaker were experimentally controlled, the peak-to-peak oscillation amplitude of the magnetic composite can be calculated as $Z_0 = \frac{a}{\omega^2}$, enabling a direct quantitative correlation between the measured V_{out} and the displacement amplitude Z_0.

3 Results and discussion

To establish a direct link between the magnetic properties of the magnetic composite and the macroscopic response of the sensing device, the results are presented following a bottom-up approach (Fig. 1). The study progresses from the synthesis and magnetic characterization of cobalt-doped ferrite MNPs, through their incorporation into polymer composites, to the simulation-assisted design of the resonant structure, its fabrication (magnetized resonant structure) by 3D printing, and the subsequent evaluation of the complete accelerometer performance.

As the first step of this bottom-up approach, the influence of magnetic remanence was addressed at the material

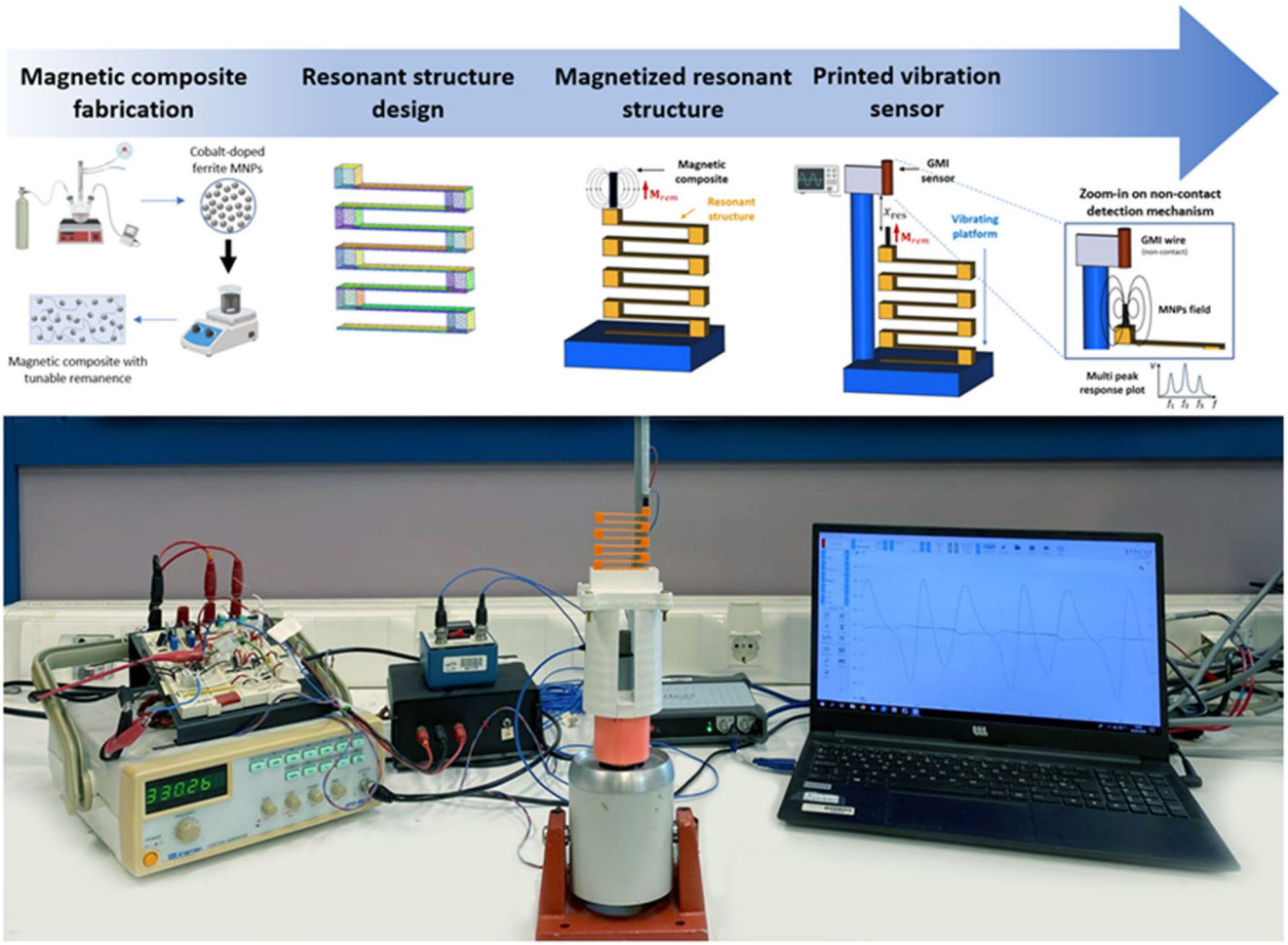


Fig. 1 **Up**: schematic overview of the design, fabrication, and operation of the multiresonant ultra-low-frequency sensing device. The figure illustrates the complete workflow followed in this work, from materials preparation to the final accelerometer system. First, cobalt-doped ferrite MNPs are synthesized and incorporated into a polymer matrix to produce a magnetic composite with tunable remanent magnetization. This composite is processed into a printable form and serves as the active magnetic material of the device. In parallel, the geometry of a flexible polymeric resonator is designed and optimized by FEM simulations to ensure that its fundamental vibration modes fall within the targeted ultra-low and low-frequency range. Based on the simulation results, the resonator is fabricated by 3D printing using a pure polymer filament, while the magnetic composite is subsequently printed to form a localized magnetized element integrated into the resonant structure. The resulting magnetized resonant structure is then combined with a GMI position sensor and dedicated signal-conditioning electronics to form the complete sensing device. Finally a detailed zoom of the magnetic based sensing scheme is provided showing multiresonant frequency behavior. **Below**: overview of the experimental assembly and testing rig

Table 1 Compositional and structural parameters of the as-synthesized MNPs and their corresponding composites, where a denotes the cell parameter, d the crystallite size, M1.5T the magnetization at 1.5 T, μ0HC the coercive field, and MR the remanent magnetization. The filling factor was calculated from the ratio between the M1.5T of the bare MNPs and that of the magnetic composite

NPs						Composite			
Stoichiometry	a (nm)	d (nm)	$M_{1.5T}$ (Am^2/kg)	μ_0H_C (mT)	M_R (Am^2/kg)	$M_{1.5T}$ (Am^2/kg)	μ_0H_C (T)	M_R (Am^2/kg)	Filling factor (%)
$Co_{0.32}Fe_{1.68}O_4$	0.8404	24	60	41	12	11	39	3	18
$Co_{0.58}Fe_{1.42}O_4$	0.8411	24	76	76	23	12	80	4	16
$Co_{0.78}Fe_{1.22}O_4$	0.8408	30	80	95	42	13	91	6	16

level through the synthesis of three batches of cobalt-doped ferrite nanoparticles, $Co_xFe_{3-x}O_4$, obtained by varying the Co/Fe precursor ratio (Table 1). The actual compositions, determined by inductively coupled plasma atomic emission spectroscopy (ICP-AES), were x = 0.32, 0.58, and 0.78. X-ray diffraction (XRD) confirmed the formation of the expected cubic spinel structure without detectable secondary phases (Fig. 2a). All samples exhibited very similar cell

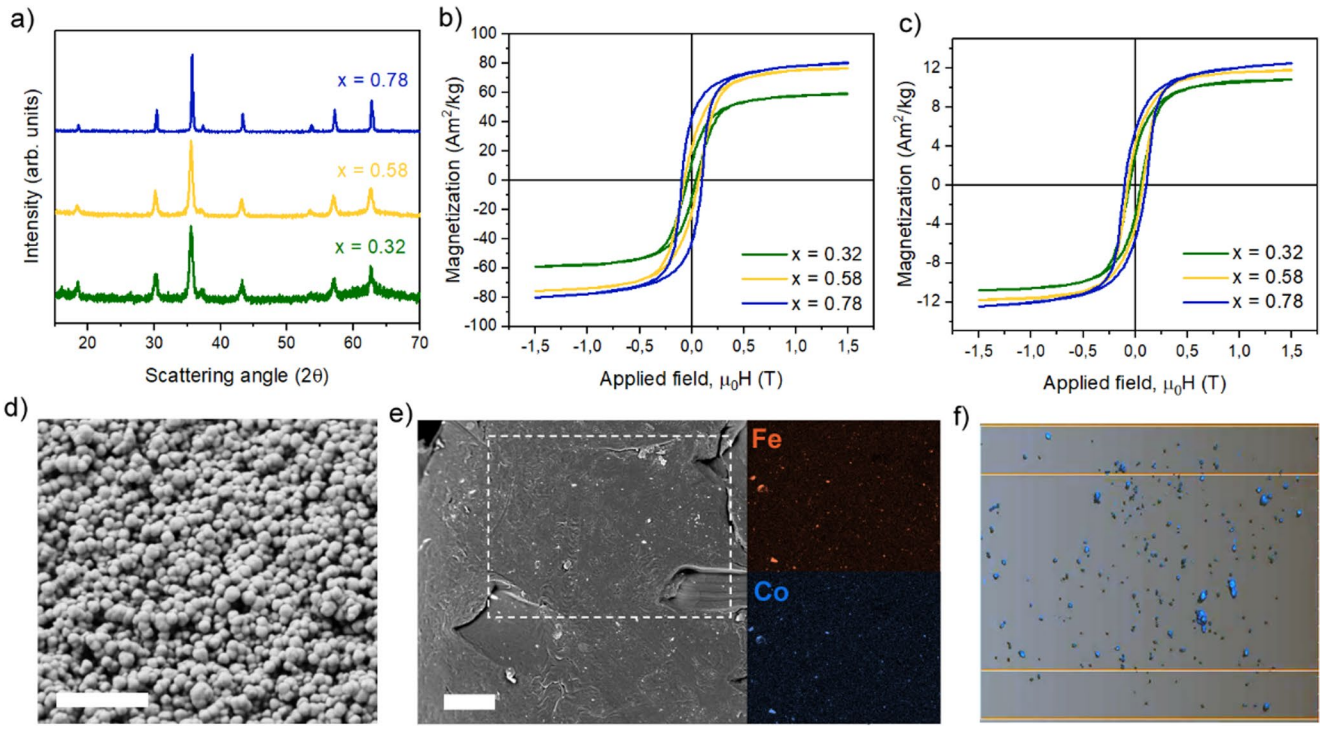


Fig. 2 **a** XRD and **b** magnetic hysteresis loops of the cobalt-doped ferrite MNPs with compositions x = 0.32, 0.58 and 0.78 ($Co_xFe_{3-x}O_4$). **c** Magnetic hysteresis loops of the corresponding magnetic composites. **d** High-resolution SEM image of the x = 0.58 MNPs (scale bar 300 nm). **e** Low-magnification SEM image of the magnetic composite prepared from x = 0.58 MNPs together with the corresponding EDX elemental maps, where Fe is shown in red and Co in blue, for the marked region (scale bar 100 μm). **f** FIB-SEM three-dimensional reconstruction of a selected volume of the x = 0.58 magnetic composite, where the blue regions highlight MNP agglomerates

parameters consistent with the reported values for cobalt-doped ferrites [61–63], and crystallite sizes between 25 and 23 nm (Table 1). Given these sizes, all samples are expected to be single-domain particles [53, 64]. Additionally, scanning electron microscopy (SEM) performed on a representative sample (x = 0.58) revealed a homogeneous particle size distribution and a morphology ranging from cubic to cuboctahedral, as typically observed for these dimensions (Fig. 2d) [64, 65]. The magnetic response recorded at room temperature confirmed ferrimagnetic behavior in all samples, as evidenced by open hysteresis loops, indicating that the nanoparticles are well below the superparamagnetic limit. While all the MNPs exhibited similar high-field magnetization values, $M_{1.5T}$, systematic increases in coercive field, H_c, and remanent magnetization, M_R, were observed as the cobalt content rose (Fig. 2b; Table 1).

The obtained MNPs were incorporated into a PCL matrix through a modified solid casting process to produce magnetic composite pellets with a fixed loading of 20 wt% for their subsequent use in fused deposition fabrication. The effective filling factor of the composites was evaluated by magnetometry, confirming that the hysteresis loops were essentially identical to those of the isolated MNPs, while the high-field magnetization was reduced to approximately 20% of the initial value (Fig. 2c; Table 1). This result indicates that the actual filling factor in the printed composites is consistent with the nominal composition, i.e., 16 to 18% (Table 1). Microstructural analysis performed by SEM combined with energy-dispersive X-ray spectroscopy (EDX) revealed a compact polymer structure with low porosity. The EDX analysis also confirmed the nanoparticle stoichiometry obtained by ICP. Regarding the morphology, a reasonably homogeneous distribution of the MNPs was observed, although a certain degree of agglomeration was present (Fig. 2e). This aggregation was more clearly evidenced by high-resolution SEM and three-dimensional focused ion beam (FIB)-SEM reconstruction, which showed clusters with characteristic sizes in the micrometer range (Fig. 2f and Supporting Information Video 1). However, this microstructural feature does not appear to significantly influence the magnetic response of the composites, since the characteristic parameters of the hysteresis loops remain practically identical to those of the original MNPs (Fig. 2b-c; Table 1).

To design a polymeric resonator capable of operating in the ultra-low and low-frequency range, first, FEM simulations were carried out to predict the mechanical response of the resonator element by estimating the resonance frequencies prior to fabrication. Initially, geometries involving cantilevers were considered and analyzed. However, in order to

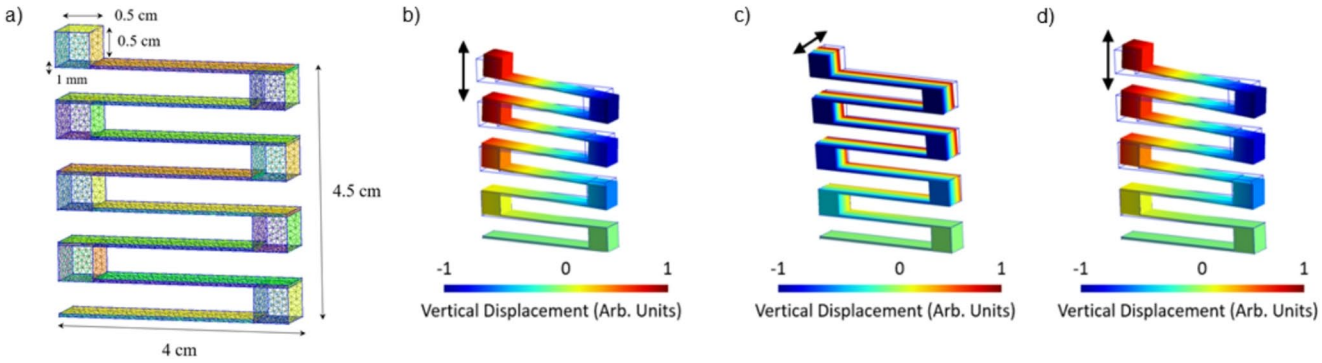


Fig. 3 **a** Schematic representation and dimensions of the FEM simulated resonator geometry. **b–d** Simulated displacement maps of the first, second and third vibration modes, respectively. The color scale corresponds to the vertical displacement along the OZ direction, expressed in arbitrary units

Table 2 Numerically, FEM, estimated (f'm).and experimental (fm) resonance frequencies

Resonance frequencies	$f\prime^{m}$(Hz) FEM ρ = 1200 kg·m⁻³	$f\prime^{m}$(Hz) FEM ρ = 840 kg·m⁻³	f^{m}(Hz) experimental
1	7.5	9.0	9.3 ± 0.6
2	12.0	14.4	13.8 ± 0.9
3	21.8	26.2	27.0 ± 1.1

reduce both the resonant frequencies and the overall size of the resonator, serpentine structures were conceived and iteratively optimized to ensure that the fundamental vibration modes fell within the targeted ultra-low-frequency region (< 10 Hz). The resulting optimized design adopted a serpentine-like architecture formed by several interconnected laminar segments. Each lamina measured 4 cm in length, 5 mm in width and 1 mm in thickness, resulting in a total height of 4.5 cm (Figs. 1 and 3a). Simulations revealed three well-defined resonant modes in the low-frequency range (up to 35 Hz) (Fig. 3b–d; Table 2). The first and third modes, appearing at 7.5 Hz and 21.8 Hz, are characterized by a vertical displacement (along the OZ direction in Fig. 3), indicating the suitability of the resonator for matching natural frequencies typically found in ultra-low and low-frequency vibration environments, respectively. The second mode, at 12.0 Hz, is mainly governed by longitudinal displacement, showing a weak vertical component.

Afterwards, the complete magnetized resonant structure, comprising the polymeric resonant structure and the magnetic composite element, was fabricated using a sequential 3D-printing process (Fig. 1). The resonator was printed in PLA following the dimensions established by the FEM simulations. Subsequently, a cylindrical magnetic composite element (7 mm in height, 3 mm in width, 4 mm in thickness) was printed on top of the polymeric resonator using the PCL-based magnetic composite (Fig. 4a). This resulted in three different magnetized resonant structures corresponding to composites containing MNPs with cobalt doping levels of x = 0.32, 0.58 and 0.78. A similar weight of 6.6 g was found for all manufactured structures. Each structure was then magnetized along the OZ direction by applying an external DC magnetic field generated by a rectangular NdFeB (dimensions 2 × 0.5 × 0.5 mm) permanent magnet with a magnetic field at its surface of 0.4 T at its pole. To ensure a correct magnetization in the OZ direction, the structures were placed in direct contact with the magnet's pole for a duration of 10 s and sequentially integrated with the GMI sensor to form the complete sensing devices, hereafter referred to as A32, A58 and A78 according to the cobalt doping level of the magnetic composite. This integration involved positioning the GMI wire directly above the magnetic composite and aligning both along the OZ axis to maximize magnetic field coupling (Figure S2). This vertical configuration allows the GMI sensor to detect variations in the vertical component of the magnetic field produced by the oscillatory motion of the magnetized resonant structure, thereby enabling vibration detection along the OZ direction (Fig. 4a). It must be noted that the GMI sensor vibrated in phase with the shaker platform and hence, resonance conditions are required to induce variations in x_{res}, the distance between the GMI sensor and the resonant structure. Under these conditions, the oscillatory motion led to cyclic variations in the magnetic field at the GMI sensor position. These variations modulate its electrical impedance, resulting in an amplitude-modulation (AM) of the current flowing through the sensor. This AM signal (Figure S3) is demodulated by a homemade analog electronic interface [23], which uses a dual passive envelope detector to extract the positive and negative envelopes. Both signals are then subtracted using a differential amplifier, leading to the output voltage signal, V_{out}, shown in Fig. 4b, whose amplitude and frequency correspond to the sensor impedance variations [23]. To assign a physical meaning to the measured V_{out} signal in terms of mechanical displacement, a calibration of the GMI sensor response was performed under non-resonant

conditions. Under these calibration conditions, a direct correlation between the measured output voltage V_{out} and the peak-to-peak oscillation amplitude of the magnetic composite element, Z_0, can be established (see methods, Sect. 2.9). From the linear fit obtained in Fig. 4b for the 20 wt% magnetic composite, described by V_{out} (V) = 0.219 Z_0 (mm) − 0.03, Z_0 can be directly extracted from the sensor signal. Once Z_0 is known, the oscillation amplitude of the vibrational source, Y_0, can be estimated through the mechanical response of the resonant structure, allowing the vibration amplitude of the monitored system to be quantitatively determined through the expression found in [23, 66].

To evaluate the dynamic performance of the final sensing device under controlled vibration conditions, the system was mounted on an electrodynamic shaker and subjected to vertical excitations while sweeping the excitation frequency in the 4–35 Hz range, at a constant peak-to-peak acceleration of 0.3 g. A clear multiresonant response was observed for all devices, with three well-defined peaks consistently located around mean values of 9.3, 13.8, and 27.0 Hz (Fig. 4c; Table 2). It should be noted that the resonance frequencies remained practically constant for each resonant structure regardless of the MNP loading or excitation acceleration. When comparing different units, maximum standard deviations of 0.6 and 1.1 Hz for the first and third modes were found, respectively, in the most unfavorable cases, representing a relative error < 7%. Moreover, these values are in good agreement with the FEM-predicted vibration modes of the resonator, although slightly shifted toward higher values (Table 2). This shift is attributed to the reduced effective density of the 3D-printed structure compared with the bulk material, a common consequence of interlayer porosity and infill settings (20% in this case) in fused-deposition-printed polymers. When a lower effective density of ρ = 840 kg·m^{-3} is considered, roughly 30% below the bulk density, the model successfully achieves a precise reproduction of the experimental results (see Table 2). This reduction is consistent with the combined effect of the unfiled interior regions, controlled by the printing infill parameters, and the additional voids and microgaps that form at the edges of printed structures. Furthermore, the relative voltage peak intensities match the vibration mode shapes (displacement fields): the first and third modes, which involve larger vertical motion of the resonant structure, yield the highest responses, whereas the second mode produces a much weaker signal due to its predominantly lateral displacement (Fig. 2c). Despite this, the GMI sensor successfully detects the weak vertical displacement associated with the second mode, demonstrating its high sensitivity. The multiresonant response of the device defines two frequency ranges of practical interest for vibration sensing, centered around the first and third resonant modes. The first operational window lies in the 8–11 Hz region, while the third mode defines a second detection band that initially spans approximately 20–30 Hz. Interestingly, this higher-frequency window shifts and broadens when the remanence of the magnetic composite element increases. In particular, for the A78 device, the third-mode window extends up to 35 Hz. In addition to shifting the operational frequency windows, the magnetic remanence also determines the strength of the detected signal. As shown in Fig. 4c, the V_{out} peak intensity increases systematically with the remanence of the embedded nanoparticles, with the A78 device exhibiting the highest response. This behavior is consistent with the larger stray magnetic fields generated by higher-remanence MNPs, which lead to more pronounced magnetic field variations at the GMI sensor.

To further evaluate the sensing capability of the device, the dynamic response of the A78 system was examined at progressively lower excitation levels, ranging from 0.05 to 0.3 g (peak-to-peak). These frequency and acceleration conditions are compatible with those found in Structural Health Monitoring (SHM) scenarios [67–72], testing the accelerometer's potential applicability for real-use applications. As shown in Fig. 4d, the device preserved its characteristic multiresonant response across all tested excitation levels, and, as expected, the amplitude of V_{out} decreased as the acceleration was reduced, reflecting the lower mechanical energy transmitted to the resonator and the consequently smaller magnetic field variations at the GMI sensor. Remarkably, even at the lowest tested acceleration of 0.05 g, the device maintained a clear resonance signature, demonstrating its ability to detect weak vibrations in the ultra-low and low-frequency range. It should be noted that measurements at accelerations below 0.05 g could not be reliably performed due to experimental setup limitations, which limit the vibration characterization at very small amplitudes.

To contextualize the device's operational response, the measured V_{out} values extracted at the maxima of the first and third resonant peaks were analyzed as a function of the input shaker acceleration. As illustrated in Fig. 4e, the resultant response became nonlinear and tended to saturate at higher accelerations, a. This behavior contrasts with the calibration results (Fig. 4b), where the same magnetized composite (20% wt without resonator) displayed a linear response across a wider acceleration range up to 3 g (note that for constant ω , the relation $Z_0 = \frac{a}{\omega^2}$ implies the same trend for amplitude and acceleration). This divergence is consistent with a reduced transmission efficiency of the polymeric resonator, indicating that the structure attenuates the vibration delivered by the source at larger excitation amplitudes. Finally, the performed 1-day stress test confirmed the device's stability, showing, after an initial stabilization period, a voltage stable signal with fluctuations

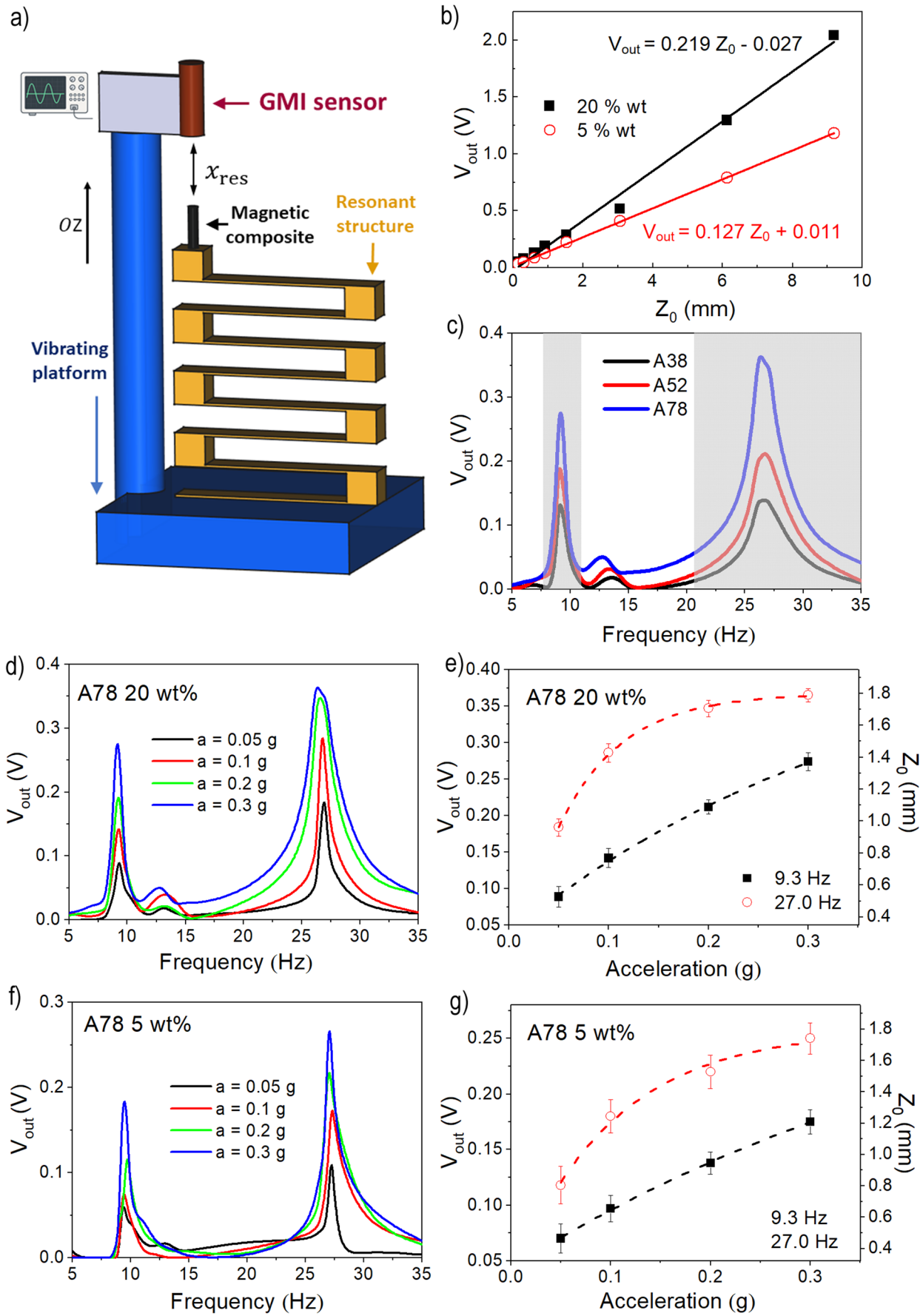

a)
GMI sensor
x_{res}
oz
Magnetic composite
Resonant structure
Vibrating platform
b)
V_{out} = 0.219 Z_0 - 0.027
20 % wt
5 % wt
V_{out} = 0.127 Z_0 + 0.011
V_{out} (V)
Z_0 (mm)
c)
A38
A52
A78
V_{out} (V)
Frequency (Hz)
d)
A78 20 wt%
a = 0.05 g
a = 0.1 g
a = 0.2 g
a = 0.3 g
V_{out} (V)
Frequency (Hz)
e)
A78 20 wt%
9.3 Hz
27.0 Hz
V_{out} (V)
Z_0 (mm)
Acceleration (g)
f)
A78 5 wt%
a = 0.05 g
a = 0.1 g
a = 0.2 g
a = 0.3 g
V_{out} (V)
Frequency (Hz)
g)
A78 5 wt%
9.3 Hz
27.0 Hz
V_{out} (V)
Z_0 (mm)
Acceleration (g)

Fig. 4 **a** Schematic representation of the complete multiresonant ultra-low-frequency sensing device. **b** Calibration curves relating the sensor output voltage V_{out} to the peak-to-peak oscillation amplitude of each magnetic composite element, Z_0, for magnetic composites with 5 and 20 wt% MNP concentrations. Solid lines represent the corresponding linear fits for each data set. **c** Multiresonant response of devices A32, A58 and A78 measured at a peak-to-peak acceleration of 0.3 g, with the shaded regions indicating the two main operational frequency windows of the system. **d**, **f** Multiresonant response of the A78 device with 20 wt% and 5 wt% magnetic nanoparticle loading, respectively, as a function of the applied acceleration. e, g) Output voltage V_{out} corresponding to the first and third resonant modes of the A78 device with 20 wt% and 5 wt% loading, respectively, as a function of the input shaker acceleration. Dashed lines are included as guides to the eye. Error bars corresponding to the standard deviation among the three analyzed resonators are included

below 2.5% and an invariant resonance frequency along the entire cycling period (see Figure S4).

An additional advantage of the proposed accelerometer architecture lies in the tunability of the magnetic composite element. Since the stray magnetic field that drives the GMI response depends directly on the remanent magnetization of the embedded MNPs, the sensing performance can be intentionally adjusted by modifying the MNP loading in the polymer matrix. This offers a practical balance between performance and cost, as MNPs are one of the main contributors to the overall material expense. For applications requiring highly sensitive vibration detection, higher loadings can be used to enhance the stray field and therefore increase the device response. Conversely, for large-scale or cost-constrained deployments, lower loadings may be employed while still preserving detectable resonance signatures. To illustrate this tunability, an additional device was fabricated using the same cobalt-doped ferrite with x = 0.78 but with a lower filling factor of 5 wt%. This device exhibits a reduced magnetic remanence (1.5 Am^2kg^{-1}) compared to the reference 20 wt% device. As observed, the resonance pattern remained essentially unchanged upon modifying the filling factor, with the two main characteristic peaks appearing at the same frequencies (Fig. 4f), although a reduction or even suppression of the second resonant peak was noticed. As expected, the intensity of the V_{out} peaks decreases with reduced MNP content, reflecting the lower stray magnetic field variations at the GMI sensor during oscillation. This reduction stems from the interplay between the magnetic filling and the GMI response. The MNP concentration determines the static bias magnetic field at the sensor's rest position, defining its specific operating point, and hence its sensitivity, $\frac{dV}{dH}$, due to the non-linear voltage-versus-magnetic field curve (V vs. H, see Figure S5). Moreover, the lower remanence of reduced loading results in smaller magnetic field variations around the operating point for the same oscillation amplitudes. This behavior is evidenced in the 5 wt% calibration curve, which maintains a linear trend described by V_{out} (V) = 0.127 Z_0 (mm) + 0.011 (Fig. 4b), thus enabling Z_0 quantification at lower loadings. Despite this, when analyzing the response of the 5 wt% device as a function of excitation acceleration under vibration tests, a behavior similar to that observed for the 20 wt% composite was obtained. In particular, a decreasing trend of V_{out} with decreasing acceleration was found. Besides, the dependence of V_{out} at the first and third resonant peaks shows a comparable tendency toward nonlinearity at higher acceleration excitation levels (Fig. 4g). This similarity further indicates that the observed attenuation and nonlinear response at larger accelerations originate from the mechanical response of the polymeric resonator rather than from the magnetic composite itself. Consequently, the tuning of the nanoparticle loading in the magnetic composite provides a straightforward strategy to balance material cost and sensing performance, enabling either low-cost large-area deployment or high-sensitivity operation depending on application requirements.

Finally, beyond the tunability provided by the magnetic filling factor, the sensing device also allows post-fabrication adjustment of its frequency response through the controlled addition of proof masses to the resonator section (Fig. 5a-b). This strategy was evaluated for the A78 device (20 wt% filling factor), demonstrating that increasing the mass attached to the magnetized resonant structure enables systematic modification of the resonant frequencies without altering the sensing mechanism. As a first example, adding a proof mass of 0.74 g (corresponding to an increase of ~11% in the total mass) resulted in a resonant response characterized by two dominant peaks, corresponding to the fundamental and third vibrational modes, shifted to lower frequencies, approximately 7 and 21 Hz (Fig. 5c), while the second mode was again reduced. When the mass was further increased to 2.00 g and an additional one of 1.50 g was attached to the opposite end of the resonator (corresponding to a total mass increase of ~ 53%), the resonator recovered the three characteristic vibrational modes observed in the original device, but all of them shifted significantly toward lower frequencies. Notably, the fundamental resonance decreased by nearly 50%, reaching values close to 4 Hz (Fig. 5d). Importantly, these shifted resonances remained clearly measurable even under low acceleration excitation (Fig. 5e-f). Resonator-related vibration attenuation was also observed despite mass addition. This confirms that the sensing mechanism remains unchanged when adding proof mass: only the resonance frequencies are modified, enabling the device to be readily reconfigured to operate in lower-frequency regimes without compromising detection capability. This post-fabrication frequency adjustability reinforces the versatility of the proposed design, enabling adaptation to different vibration environments

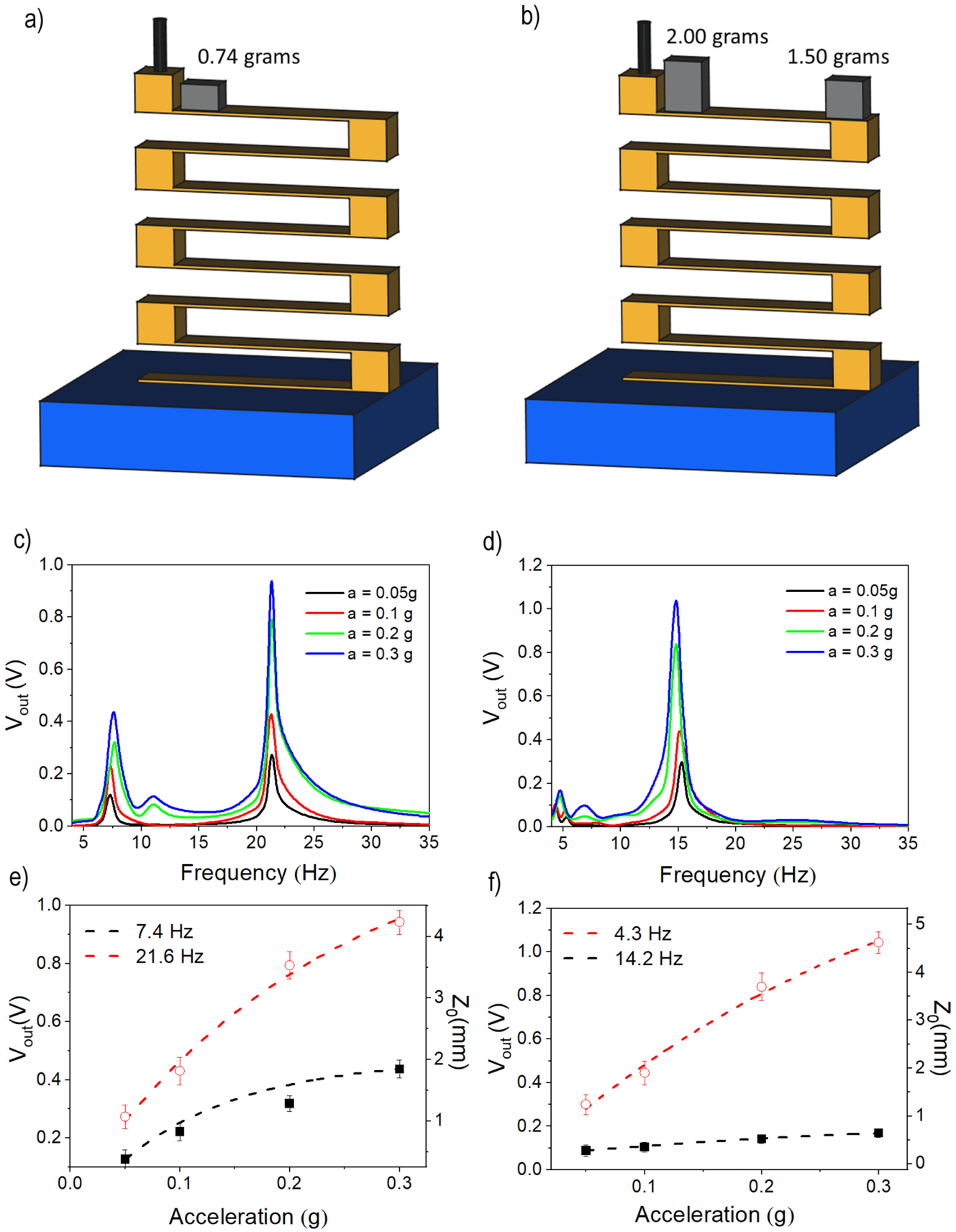

a)
0.74 grams
b)
2.00 grams
1.50 grams
c)
V_{out} (V)
a = 0.05g
a = 0.1 g
a = 0.2 g
a = 0.3 g
Frequency (Hz)
d)
V_{out} (V)
a = 0.05g
a = 0.1 g
a = 0.2 g
a = 0.3 g
Frequency (Hz)
e)
7.4 Hz
21.6 Hz
V_{out}(V)
Z_0(mm)
Acceleration (g)
f)
4.3 Hz
14.2 Hz
V_{out} (V)
Z_0(mm)
Acceleration (g)

Fig. 5 Schematic representation of the multiresonant ultra-low-frequency sensing device with added proof masses of **a** 0.74 g and **b** 2.00+1.50 g. **c**, **d** Corresponding multiresonant responses of the devices with 0.74 g and 2.00+1.50 g proof masses, respectively. **e**, **f** Output voltage V_{out} associated with the first and third resonant modes as a function of the input shaker acceleration for the devices with 0.74 g and 2.00+1.50 g proof masses, respectively. Dashed lines are included as guides to the eye. The resonant modes measured when proof masses are added are in good agreement with those theoretically predicted by FEM simulations. Error bars corresponding to the standard deviation among the three analyzed resonators are included. The resonant modes measured when proof masses are added are in good agreement with those theoretically predicted by FEM simulations

and expanding its applicability to structural health monitoring scenarios where low-frequency vibrational signatures are critical.

To evaluate the performance of the proposed magneto-mechanical vibration sensor, a quantitative comparison with current commercial and research standards is presented in Table S1 and Figure S6. Currently, IEPE accelerometers are the most widely employed commercial solutions. However, the lower the minimum measurable frequency, the higher the mass and cost of the device. Models with detection capacity well below 1 Hz necessitate either bulky proof masses and/or significant financial investment. More compact devices, exhibiting a cut-off frequency between 0.5 and 1 Hz, comparable although lower than our magneto-mechanical proposal, still involve a high cost (around hundreds of euros). Alternatively, polymeric PVDF sensors are extensively reported in the literature, primarily targeting flexible and wearable applications. Commercial sensors can operate close to 1 Hz, although they require high input impedance conditioning whose design is challenging in terms of sensitivity and signal-to-noise ratio (SNR). Furthermore, both IEPE and PVDF sensors must be physically attached to the vibrating system, leading to mechanical wear and fatigue over time.

In contrast, the proposed magneto-mechanical vibration sensor introduces a distinct scenario that does not face the theoretical detection limits of piezoelectric-based systems, showing a 4.3 Hz limit comparable to several industrial standards through a cost-efficient design. Despite this, certain challenges remain to achieve industrial maturity, including device miniaturization, spectral range expansion, and long-term fatigue characterization of the polymeric structure. Nevertheless, the combination of post-fabrication tunability, contactless transduction, and cost-effectiveness positions this platform as a potential alternative solution for ultra-low and low-frequency vibration characterization.

4 Conclusions

The feasibility of fabricating functional composite materials for the integrated manufacturing of resonant polymer-based magnetic accelerometers has been demonstrated. The proposed devices combine additive manufacturing with Giant Magnetoimpedance sensing, enabling the development of fully 3D-printed, contactless vibration sensors. A series of prototypes embedding cobalt-doped ferrite magnetic nanoparticles with tailored remanent magnetization and filling factors were fabricated, achieving reliable vibration detection down to 0.05 g within the ultra-low and low-frequency range.

These operational requirements were addressed by utilizing the low Young modulus of the polymeric matrices and the geometric versatility of 3D printing to overcome the design constraints of conventional resonant systems in the ultra-low-frequency regime. This approach was supported by a simulation-assisted design based on the Finite Element Method, which enabled the precise tuning of the fundamental resonance modes before fabrication in the required frequency range. Close agreement between numerical simulations and experimental measurements confirms the effectiveness of the proposed design strategy.

Beyond structural design, the sensing performance was effectively tuned through the magnetic properties of the embedded element. Increasing the intrinsic remanent magnetization of the cobalt-doped ferrite nanoparticles enhances the detected signal without modifying the mechanical response, while variations in the magnetic filling factor provide a direct means to balance sensitivity and material cost. Importantly, the multiresonant response is preserved across different magnetic loadings, demonstrating the decoupling between magnetic tuning and mechanical functionality. This functional versatility was further extended through post-fabrication reconfigurability, where the controlled addition of proof masses allowed the fundamental resonance to be shifted to frequencies as low as 4.3 Hz, adapting the device to diverse vibration environments without requiring re-fabrication.

Overall, the proposed 3D-printed GMI-based accelerometer provides a low-cost and adaptable platform for vibration characterization at ultra-low and low frequencies. Its multiresonant operation, reliable response at low acceleration levels, magnetic tunability, and post-fabrication reconfigurability enable flexible adaptation to different vibration scenarios, positioning this approach as a potential solution for applications requiring scalable sensing architectures and sensitivity to ultra-low and low-frequency vibrations.

Supplementary Information The online version contains supplementary material available at https://doi.org/10.1007/s42114-026-01831-6.

Acknowledgements Authors acknowledge the use of instrumentation as well as the technical advice provided by the National Facility ELECMI ICTS, node División de Microscopía Electrónica (DME) at Universidad de Cádiz (UCA). The authors also want to acknowledge Prof. M. Vázquez (ICMM, Madrid, Spain) for kindly supplying the soft magnetic wires.

Author contributions Author contribution J. G. H.: investigation, data curation, formal analysis, writing review & editing; D. L.: investigation, data curation, formal analysis, writing review & editing; I. R. S.: conceptualization, software, data curation, formal analysis, writing review & editing; D. G.: software, data curation, formal analysis, writing review & editing; J. M. A. M.: data curation, formal analysis, writing review & editing J. H. S.: resources, data curation, formal analysis, writing review & editing; C. G. P.: data curation, formal analysis, funding acquisition, writing review & editing; E. G.: conceptualization, data curation, formal analysis, methodology, software, validation and writing original draft, review & editing; (A) L. O.: conceptualization, data curation, formal analysis, funding acquisition, methodology, validation and writing original draft, review & editing; J. J. (B) L. : conceptualization, data curation, formal analysis, methodology, resources, validation and writing original draft, review & editing.

Funding Open Access funding provided by Universidad Pública de Navarra. This work is funded by Spanish Agencia Estatal de Investigación and Ministerio de Ciencia e Innovación MCIN/AEI/ https://doi.org/10.13039/501100011033 and by "European Union NextGenerationEU/PRTR", project TED2021–130884B-I00. D.L. acknowledges the EU's Horizon 2020 - Marie-Sklodowska Curie action (grant agreement No 101034285). A.L.O. acknowledges financial support from the grant CNS2022-135787 funded by MCIN/AEI /https://doi.org/10.13039/501100011033 and European Union NextGenerationEU/PRTR) and PID2024-160292OB-I00 funded by MCIU/AEI/https://doi.org/10.13039/501100011033/FEDER, UE.

Data availability The data are available from the corresponding author upon reasonable request.

Declarations

Competing interests The authors declare no competing interests.

Open Access This article is licensed under a Creative Commons Attribution 4.0 International License, which permits use, sharing, adaptation, distribution and reproduction in any medium or format, as long as you give appropriate credit to the original author(s) and the source, provide a link to the Creative Commons licence, and indicate if changes were made. The images or other third party material in this article are included in the article's Creative Commons licence, unless indicated otherwise in a credit line to the material. If material is not included in the article's Creative Commons licence and your intended use is not permitted by statutory regulation or exceeds the permitted use, you will need to obtain permission directly from the copyright holder. To view a copy of this licence, visit http://creativecommons.org/licenses/by/4.0/.

References

1. Zhong K, Liu Z, Wang F (2023) Development of CO2 curable 3D printing materials. Additive Manuf 65:103442. https://doi.org/10.1016/j.addma.2023.103442
2. Jandyal A, Chaturvedi I, Wazir I et al (2022) 3D printing – A review of processes, materials and applications in industry 4.0. Sustainable Oper Computers 3:33–42. https://doi.org/10.1016/j.susoc.2021.09.004
3. Ma T, Zhang Y, Ruan K et al (2024) Advances in 3D printing for polymer composites: A review. InfoMat 6:e12568. https://doi.org/10.1002/inf2.12568
4. Ree BJ (2024) Critical review and perspectives on recent progresses in 3D printing processes, materials, and applications. Polymer 308:127384. https://doi.org/10.1016/j.polymer.2024.127384
5. Singh N, Sinha P, Sinha DK, Banerjee S (2025) Smart polymers for 3D printing applications: current status and future outlook. Polym Chem 16:4479–4523. https://doi.org/10.1039/D5PY00741K
6. Alarifi IM (2024) Revolutionising fabrication advances and applications of 3D printing with composite materials: a review. Virtual Phys Prototyp 19:e2390504. https://doi.org/10.1080/17452759.2024.2390504
7. Wang S, Chen X, Han X et al (2023) A Review of 3D Printing Technology in Pharmaceutics: Technology and Applications. Now Future Pharm 15:416. https://doi.org/10.3390/pharmaceutics15020416
8. Bodkhe S, Vigo L, Zhu S et al (2020) 3D PRINTING TO INTEGRATE ACTUATORS INTO COMPOSITES. Additive Manuf 35:101290. https://doi.org/10.1016/j.addma.2020.101290
9. Wolstrup AF, Spangenberg J, Yamamoto A et al (2025) Advances in 3D printed electromechanical sensors: Performance comparison, trends, and future directions. Additive Manuf 106:104799. https://doi.org/10.1016/j.addma.2025.104799
10. Ehrmann G, Blachowicz T, Ehrmann A (2022) Magnetic 3D-Printed Composites—Production and Applications. Polymers 14:3895. https://doi.org/10.3390/polym14183895
11. Galarreta-Rodriguez I, Lopez-Ortega A, Garayo E et al (2023) Magnetically activated 3D printable polylactic acid/polycaprolactone/magnetite composites for magnetic induction heating generation. Adv Compos Hybrid Mater 6:102. https://doi.org/10.1007/s42114-023-00687-4
12. Zhai H, Li X, Yu S et al (2025) Review on the 3D printing technology and application of magnetic materials: Material-process-structure-application. Compos Part B: Eng 298:112387. https://doi.org/10.1016/j.compositesb.2025.112387
13. Selema A, Beretta M, Van Coppenolle M et al (2023) Evaluation of 3D-Printed Magnetic Materials For Additively-Manufactured Electrical Machines. J Magn Magn Mater 569:170426. https://doi.org/10.1016/j.jmmm.2023.170426
14. Kandasubramanian GK B (2022) Exertions of Magnetic Polymer Composites Fabricated via 3D Printing. Ind Eng Chem Res 61:16895–16909. https://doi.org/10.1021/acs.iecr.2c02299
15. Sun R, Zhou S, Cheng L (2023) Ultra-low frequency vibration energy harvesting: Mechanisms, enhancement techniques, and scaling laws. Energy Conv Manag 276:116585. https://doi.org/10.1016/j.enconman.2022.116585
16. Masara DO, El Gamal H, Mokhiamar O (2021) Split Cantilever Multi-Resonant Piezoelectric Energy Harvester for Low-Frequency Application. Energies 14:5077. https://doi.org/10.3390/en14165077
17. Hayakawa M, Hattori K, Ohta K (2007) Monitoring of ULF (Ultra-Low-Frequency) Geomagnetic Variations Associated with Earthquakes. Sensors 7:1108–1122. https://doi.org/10.3390/s7071108
18. Liu H, Lee C, Kobayashi T et al (2012) A new S-shaped MEMS PZT cantilever for energy harvesting from low frequency vibrations below 30 Hz. Microsyst Technol 18:497–506. https://doi.org/10.1007/s00542-012-1424-1

19. Mohd Ghazali MH, Rahiman W (2021) Vibration Analysis for Machine Monitoring and Diagnosis: A Systematic Review. Shock Vib 2021:9469318. https://doi.org/10.1155/2021/9469318
20. Royo-Silvestre I, Beato-López JJ, Gómez-Polo C (2024) Optimization procedure of low frequency vibration energy harvester based on magnetic levitation. Appl Energy 360:122778. https://doi.org/10.1016/j.apenergy.2024.122778
21. Wang T, Cui T, Qi X, Huan X (2025) Urban Viaduct Structural Health Monitoring: A Review of Wireless Sensor Approaches. Buildings 15:1619. https://doi.org/10.3390/buildings15101619
22. Khan FU, Iqbal M (2018) Electromagnetic Bridge Energy Harvester Utilizing Bridge's Vibrations and Ambient Wind for Wireless Sensor Node Application. J Sens 2018:3849683. https://doi.org/10.1155/2018/3849683
23. Beato-López JJ, Royo-Silvestre I, Algueta-Miguel JM, Gómez-Polo C (2020) A Combination of a Vibrational Electromagnetic Energy Harvester and a Giant Magnetoimpedance (GMI) Sensor. Sensors 20:1873. https://doi.org/10.3390/s20071873
24. Royo-Silvestre I, Beato-López JJ, Algueta-Miguel JM, Gómez-Polo C (2025) Ultra low frequency vibrations. In: Reference Module in Earth Systems and Environmental Sciences. Encyclopedia of the Anthropocene (Second Edition) Elsevier: 180–197
25. Kołakowski P (2007) Structural Health Monitoring – a Review with the Emphasis on Low-Frequency Methods. Eng Trans 55:239
26. Wu T, Liu G, Fu S, Xing F (2020) Recent Progress of Fiber-Optic Sensors for the Structural Health Monitoring of Civil Infrastructure. Sensors 20:4517. https://doi.org/10.3390/s20164517
27. Azhar AS, Kudus SA, Jamadin A et al (2024) Recent vibration-based structural health monitoring on steel bridges: Systematic literature review. Ain Shams Eng J 15:102501. https://doi.org/10.1016/j.asej.2023.102501
28. Chu T, Nguyen T, Yoo H, Wang J (2024) A review of vibration analysis and its applications. Heliyon 10. https://doi.org/10.1016/j.heliyon.2024.e26282
29. Hassan MF, Li Z, Islam MS et al (2025) Wireless Printed Large-Area Sensors for Continuous Structural Health Monitoring. Adv Mater Technol 10:2401782. https://doi.org/10.1002/admt.202401782
30. Dai J, Li M, Chen H et al (2022) Progress and challenges on blade load research of large-scale wind turbines. Renewable Energy 196:482–496. https://doi.org/10.1016/j.renene.2022.07.017
31. Wu T, You D, Gao H et al (2023) Research status and development trend of piezoelectric accelerometer. Crystals 13. https://doi.org/10.3390/cryst13091363
32. Ma L, Li Z, Yang S, Wang J (2025) A review on vibration sensor: key parameters, fundamental principles, and recent progress on industrial monitoring applications. Vibration 8. https://doi.org/10.3390/vibration8040056
33. D'Emilia G, Gaspari A, Natale E (2019) Amplitude–phase calibration of tri-axial accelerometers in the low-frequency range by a LDV. J Sens Sens Syst 8:223–231. https://doi.org/10.5194/jsss-8-223-2019
34. Mardanshahi A, Sreekumar A, Yang X et al (2025) Sensing Techniques for Structural Health Monitoring: A State-of-the-Art Review on Performance Criteria and New-Generation Technologies. Sens (Basel) 25:1424. https://doi.org/10.3390/s25051424
35. Zhang LS, Liu YB, Pan CL, Feng ZH (2013) Leakage current characterization and compensation for piezoelectric actuator with charge drive. Sens Actuators A: Phys 199:116–122. https://doi.org/10.1016/j.sna.2013.05.014
36. Zare Pakzad S, Egger P, Rahnemai Haghighi N et al (n.d.) Modeling and measurement of noise in aluminium nitride piezoelectric MEMS. Adv Electron Mater n/a:e00476. https://doi.org/10.1002/aelm.202500476
37. Li H, Tian C, Deng ZD (2014) Energy harvesting from low frequency applications using piezoelectric materials. Appl Phys Rev 1:041301. https://doi.org/10.1063/1.4900845
38. Elvin NG, Elvin AA (2011) An experimentally validated electromagnetic energy harvester. J Sound Vib 330:2314–2324. https://doi.org/10.1016/j.jsv.2010.11.024
39. Covaci C, Gontean A (2020) Piezoelectric Energy Harvesting Solutions: A Review. Sensors 20:3512. https://doi.org/10.3390/s20123512
40. Das S, Jain N, Saha A (2024) Noncontact Self-Vibration Compensated Position Sensitive Detector Based Low-Frequency Vibration Measurement. IEEE Trans Instrum Meas 73:1–8. https://doi.org/10.1109/TIM.2024.3367381
41. Kumar N, Kurchania R, Ball RJ et al (2024) Enhanced dielectric, ferroelectric and piezoelectric properties of lead-free (Ba,Ca)(Sn,Ti)O3 ceramics by optimisation of sintering temperature. J Alloys Compd 989:174358. https://doi.org/10.1016/j.jallcom.2024.174358
42. Jonscher C, Hofmeister B, Grießmann T, Rolfes R (2022) Very low frequency IEPE accelerometer calibration and application to a wind energy structure. Wind Energy Sci 7:1053–1067. https://doi.org/10.5194/wes-7-1053-2022
43. Ge C, Cretu E (2024) Polymeric piezoelectric accelerometers with high sensitivity, broad bandwidth, and low noise density for organic electronics and wearable microsystems. Microsyst Nanoeng 10:61. https://doi.org/10.1038/s41378-024-00704-6
44. Ge C, Cretu E (2023) A polymeric piezoelectric MEMS accelerometer with high sensitivity, low noise density, and an innovative manufacturing approach. Microsyst Nanoeng 9:151. https://doi.org/10.1038/s41378-023-00628-7
45. Kalimuldina G, Turdakyn N, Abay I et al (2020) A review of piezoelectric PVDF film by electrospinning and its applications. Sensors 20. https://doi.org/10.3390/s20185214
46. Wang Y, Lei D, Wu L et al (2023) Effects of stretching on phase transformation of PVDF and its copolymers: a review. Open Phys 21. https://doi.org/10.1515/phys-2022-0255
47. Gong X, Kuo Y-C, Zhou G et al (2023) An aerosol deposition based MEMS piezoelectric accelerometer for low noise measurement. Microsyst Nanoeng 9:23. https://doi.org/10.1038/s41378-023-00484-5
48. Phan M-H, Peng H-X (2008) Giant magnetoimpedance materials: Fundamentals and applications. Prog Mater Sci 53:323–420. https://doi.org/10.1016/j.pmatsci.2007.05.003
49. Beato-López JJ, Algueta-Miguel JM, Gómez-Polo C (2021) Contactless magnetic nanoparticle detection platform based on nonlinear GMI effect. Measurement 180:109602. https://doi.org/10.1016/j.measurement.2021.109602
50. Beato-López JJ, Algueta-Miguel JM, Galarreta-Rodriguez I et al (2022) Magnetic binary encoding system based on 3D printing and GMI detection prototype. Sens Actuators A: Phys 347:113946. https://doi.org/10.1016/j.sna.2022.113946
51. Beato-López JJ, Algueta-Miguel JM, Galarreta-Rodriguez I et al (2023) Non-linear GMI decoding in 3D printed magnetic encoded systems. Sens Actuators A: Phys 358:114447
52. Constantinou P, Roy S (2015) A non-linear 3D printed electromagnetic vibration energy harvester. J Phys: Conf Ser 660:012092. https://doi.org/10.1088/1742-6596/660/1/012092
53. Liguori D, Muzzi B, Innocenti C et al (2026) Revealing the intrinsic magnetic landscape of cobalt-doped ferrite nanoparticles. Mater Today Nano 33:100775. https://doi.org/10.1016/j.mtnano.2026.100775
54. Diffraction M-, MAU MAUD - (2025) Materials analysis using diffraction (and more). In: MAUD - materials analysis using diffraction (and more). https://luttero.github.io/maud/. Accessed 30 Oct

55. Lopez-Dominguez V, Quesada A, Guzmán-Mínguez JC et al (2018) A simple vibrating sample magnetometer for macroscopic samples. Rev Sci Instrum 89:034707. https://doi.org/10.1063/1.5017708
56. Zienkiewicz OC, Taylor RL, Zhu JZ (2005) The finite element method: its basis and fundamentals
57. Bower AF (2009) Applied Mechanics of Solids. CRC, Boca Raton
58. Larson MG, Bengzon F (2013) The Finite Element Method: Theory, Implementation, and Applications. Springer, Berlin, Heidelberg
59. Sundarasetty H, Sahu SK (2025) Experimental and Computational Study on the Tensile and Flexural Properties of Polylactic Acid filled with Boron Nitride Nanoplatelets. Fract Struct Integr 19:211–224. https://doi.org/10.3221/IGF-ESIS.72.15
60. Das TK, Mitra A, Mandal SK et al (2014) Parametric controls on giant magnetoimpedance (GMI) behaviour of CoFeSiBCr amorphous wires for prospective sensor applications. Sens Actuators A: Phys 220:382–387. https://doi.org/10.1016/j.sna.2014.10.027
61. Jeon S-H, Son Y-H, Choi W-I et al (2018) Simulating Porous Magnetite Layer Deposited on Alloy 690TT Steam Generator Tubes. Materials 11:62. https://doi.org/10.3390/ma11010062
62. Jasrotia R, Prakash J, Saddeek YB et al (2025) Cobalt ferrites: Structural insights with potential applications in magnetics, dielectrics, and Catalysis. Coord Chem Rev 522:216198. https://doi.org/10.1016/j.ccr.2024.216198
63. Ansari SM, Younis A, Kolekar YD, Ramana CV (2025) Cobalt ferrite nanoparticles: The physics, synthesis, properties, and applications. Appl Phys Rev 12:021308. https://doi.org/10.1063/5.0244555
64. López-Ortega A, Lottini E, Fernández C, de Sangregorio J C (2015) Exploring the Magnetic Properties of Cobalt-Ferrite Nanoparticles for the Development of a Rare-Earth-Free Permanent Magnet. Chem Mater 27:4048–4056. https://doi.org/10.1021/acs.chemmater.5b01034
65. Muzzi B, Lottini E, Yaacoub N et al (2022) Hardening of Cobalt Ferrite Nanoparticles by Local Crystal Strain Release: Implications for Rare Earth Free Magnets. ACS Appl Nano Mater 5:14871–14881. https://doi.org/10.1021/acsanm.2c03161
66. Zhang Q, Kim ES (2014) Vibration energy harvesting based on magnet and coil arrays for watt-level handheld power source. Proceedings of the IEEE 102:1747–1761. https://doi.org/10.1109/JPROC.2014.2358995
67. Janeliukstis R, Ratnika L, Gaile L, Rucevskis S (2025) Environmental Factors in Structural Health Monitoring—Analysis and Removal of Effects from Resonance Frequencies. J Sens Actuator Networks 14:33. https://doi.org/10.3390/jsan14020033
68. Dong Y, Fagert J, Noh HY (2023) Characterizing the variability of footstep-induced structural vibrations for open-world person identification. Mech Syst Signal Process 204:110756. https://doi.org/10.1016/j.ymssp.2023.110756
69. Górski P, Napieraj M, Konopka E (2020) Variability evaluation of dynamic characteristics of highway steel bridge based on daily traffic-induced vibrations. Measurement 164:108074. https://doi.org/10.1016/j.measurement.2020.108074
70. Zini G, Betti M, Bartoli G (2022) Experimental analysis of the traffic-induced-vibration on an ancient lodge. Struct Control Health Monit 29:e2900. https://doi.org/10.1002/stc.2900
71. Matsuoka K, Collina A, Somaschini C, Sogabe M (2019) Influence of local deck vibrations on the evaluation of the maximum acceleration of a steel-concrete composite bridge for a high-speed railway. Eng Struct 200:109736. https://doi.org/10.1016/j.engstruct.2019.109736
72. Ahmadi E, Kashani MM (2020) Numerical investigation of nonlinear static and dynamic behaviour of self-centring rocking segmental bridge piers. Soil Dyn Earthq Eng 128:105876. https://doi.org/10.1016/j.soildyn.2019.105876

Publisher's note Springer Nature remains neutral with regard to jurisdictional claims in published maps and institutional affiliations.